Supporting Information

# Anisotropic material depletion in epitaxial polymer crystallization

Jason X. Liu,[†,‡] Yang Xia,[†] Yucheng Wang,[¶] Mikko P. Haataja,[†,‡] Craig B. Arnold,[†,‡] and Rodney D. Priestley[*,¶,‡]

†Department of Mechanical and Aerospace Engineering, Princeton University, Princeton, NJ 08540, USA

‡Princeton Materials Institute, Princeton University, Princeton, NJ 08540, USA

¶Department of Chemical and Biological Engineering, Princeton University, Princeton, NJ 08540, USA

E-mail: rpriestl@princeton.edu

## Contents

## 1. Materials

DI water was filtered through a 0.2 $\mu$m filter using a NANOpure Diamond filtration system. Polyethylene oxide (PEO) ($M_w = 12 \times 10^3$ g/mol) was purchased from Sigma Aldrich. Muscovite mica, V1 grade, was purchased from Ted Pella. Silicon wafers (P-type, boron dopant, <100> orientation) were purchased from University Wafer and used as received.

## 2. Experimental methods

To perform MAPLE depositions, we first prepared laser ablation targets by dissolving PEO into water at a mass concentration of 0.5% wt. About 10 mL of aqueous solution was transferred to an aluminum target cup and rapidly frozen in a liquid nitrogen (LN2) bath. The frozen target was subsequently transferred into the MAPLE deposition vacuum chamber and maintained at LN2 temperatures with a cryogenic cooling system. Substrates were loaded through a load-lock chamber and inserted into the main chamber at a distance of 70 mm from the ablation target surface. Muscovite mica samples were freshly cleaved prior to use and Si wafers were used as-received. Laser ablation was performed with an Er:YAG laser (Pantec DPM-25 Medical Laser) operating at a wavelength of $\lambda = 2940$ nm. Depositions were performed with a laser repetition rate of 10 Hz, pulse duration of 250 $\mu$s and laser fluence of 1.7 J/cm$^2$. The vacuum chamber was pumped to a base pressure of $5 \times 10^{-5}$ Torr before a deposition was started, and when laser ablation was initiated, the chamber pressure rose to a pressure of $1 \times 10^{-4}$ Torr. During laser ablation, the frozen aqueous PEO target was rotated at 1 Hz and the laser beam was rastered across the sample to prevent excessive local melting. The substrates were rotated at 1 Hz to ensure a uniform deposition. The substrate was maintained at 20 °C unless otherwise specified, with a heat lamp in conjunction with a substrate temperature sensor. All depositions were performed for 1.5 minutes, to achieve a structured film comprised of a distribution of globule sizes.

Atomic force microscopy (AFM) was performed in tapping mode at room temperature with a Bruker Dimension ICON3 AFM. All AFM measurements were performed with Bruker tips, model RTESP, with spring constant $k = 40$ N/m and resonant frequency $f_0 = 300$ kHz. AFM image analysis was performed using Gwyddion.

Transmission electron microscopy (TEM) and selected area electron diffraction (SAED) was performed on a Titan Cubed Themis 300 TEM operating at 300 kV.

The software package Vesta (JP-Minerals)[1] was used to generate atomic models of the crystal structures.

# 3. Simulation Methods

The total free energy functional, $F$, for the 2D case is

$$F = \int \{\epsilon_{tot}[(\nabla \cdot \phi)^2 + |\nabla \times \phi|^2] + \epsilon_h |\nabla^2 \phi|^2 + f(\phi, u)\} dr \tag{1}$$

$$f(\phi, u) = \frac{1 + b_1[c_1 h(\theta) + (1 - c_1) \cos(24\theta)] \sin^2 \varphi}{4(1 + b_1)} \frac{1 + b_2 \cos(4\varphi)}{1 + b_2} |\phi|^4$$

$$+ \frac{m(u) - \frac{3}{2} - \tilde{\lambda} \cos^2 \varphi}{3} |\phi|^3 - \frac{m(u) - \frac{1}{2} - \tilde{\lambda} \cos^2 \varphi}{2} |\phi|^2 \tag{2}$$

$$m(u) = \frac{\alpha}{\pi} \arctan(-\gamma u) \tag{3}$$

$$\tilde{\lambda} = \lambda + \frac{3 b_1}{2(1 + b_1)} \tag{4}$$

$$h(\theta) = -\exp[-\frac{\theta^2}{0.005}] - \exp[-\frac{(\theta - \frac{\pi}{3})^2}{0.005}] - \exp[-\frac{(\theta - \frac{2\pi}{3})^2}{0.005}] - \exp[-\frac{(\theta - \pi)^2}{0.005}]$$

$$- \exp[-\frac{(\theta + \frac{\pi}{3})^2}{0.005}] - \exp[-\frac{(\theta + \frac{2\pi}{3})^2}{0.005}] - \exp[-\frac{(\theta + \pi)^2}{0.005}] \tag{5}$$

$$\epsilon_{tot} = \frac{\epsilon^2}{2} \{1 - [\epsilon_4 \frac{(\phi \cdot n)^4}{|\phi|^4 |n|^4} - \epsilon_2 \frac{(\phi \cdot n)^2}{|\phi|^2 |n|^2}]\} \tag{6}$$

with the following constraints on parameter values:

$$0 < \alpha < 1, \quad -\frac{1}{2} + \frac{3 b_1}{1 + b_1} + |\tilde{\lambda}| < m < \frac{1}{2} - |\tilde{\lambda}|, \quad and \quad -1 < b_2 < 0. \tag{7}$$

$\varphi$ is the angle between $\phi$ and the $z$ axis. $\varphi = 90°$ corresponds to the edge-on orientation while $\varphi = 0°$ corresponds to flat-on. $\theta$ denotes the angle between the projection of $\phi$ onto $x - y$ plane and the $y$ axis. By having the constraint in Eq. 7, the local minimum of the bulk free energy $f(\phi, u)$ will maintain $|\phi| = 0$ and 1 as well as $\varphi = 0°$ and $90°$. The relative depth of the double-well $f(\phi, u)$ is controlled by $\lambda$ and $m(u)$. Here $m(u)$ is a function of $u$ such that the energy difference between the amorphous ($|\phi| = 0$) and crystalline ($|\phi| = 1$) phase is related to $u$ and thus the crystallization will stop when $u \to 0$. The six-fold symmetric anisotropy of the bulk free energy with respect to $\theta$, coming from the substrate interaction, is incorporated by $h(\theta)$ with $b_1$ and $c_1$ to adjust the amplitude of this anisotropy. In addition to this six-fold symmetry, a 24-fold symmetry of $\theta$ dependence is also introduced to make certain in-plane misorientation to be preferred at grain boundaries. Parameter $b_2$ is related to the energy barrier between the edge-on ($\varphi = 90°$) and flat-on ($\varphi = 0°$) orientations.

For the interfacial energy, the interfacial energy related parameter $\epsilon_{tot}$ is anisotropic with respect to the angle between $\phi$ and growth front (i.e. the crystal/amorphous interface) normal vector $n$. By using the second and fourth order $\frac{\phi \cdot n}{|\phi||n|}$ term, we can modulate the Wulff

3

plot to a faceted quadrilateral with the length and width controlled by $\epsilon_2$ and $\epsilon_4$. However, strong anisotropic (nonconvex) surface free energy densities can cause numerical problems or lead to a dynamically unstable problem. Therefore, we use Torabi *et al.* 's method to smooth the interfacial energy at the corner by adding an isotropic high order gradient $|\nabla^2\phi|^2$. Specifically, the preparameter of this gradient $\epsilon_h$ is set to be relatively small such that it will only convexify the interface at the corner.

We employ the following evolution equations to advance the crystal growth morphology in time.

$$\frac{\partial \phi_x}{\partial t} = -M\frac{\delta F}{\delta \phi_x} + \eta_x \tag{8}$$

$$\frac{\partial \phi_y}{\partial t} = -M\frac{\delta F}{\delta \phi_y} + \eta_y \tag{9}$$

$$\frac{\partial \phi_z}{\partial t} = -M\frac{\delta F}{\delta \phi_z} + \eta_z \tag{10}$$

$$\frac{\partial u}{\partial t} = D_u\nabla^2 u + \frac{1}{\Delta}\frac{\partial |\phi|}{\partial t} \tag{11}$$

$\Delta$ is a parameter related to the densification process during the crystallization due to the difference of density and thickness between the crystalline and amorphous phase. Specifically, for a uniform system with $\Delta < 1$, the maximum fraction of system that can be crystallized will be $\Delta$. In our 2D system, in order to phenomenologically reflect the fact that the thin film region will condense due to the crystallization while the thick droplet not, we use a densification parameter of $\Delta = 2$ within the droplet and $\Delta = 0.5$ in the thin film region. $M$ is the mobility given by

$$M = \tilde{M}[(1 - |\frac{\phi \cdot n}{|\phi||n|}|)\sin^2\varphi][1 + \delta_\beta(1 + \cos(k\psi))\cos^2\varphi] \tag{12}$$

$$\tilde{M} = M_{max}\frac{1}{2}(1 + \tanh(-\frac{|\phi| - \bar{c}}{\tilde{c}})) \tag{13}$$

$$\psi = \tan^{-1}(\frac{\partial |\phi|}{\partial y}/\frac{\partial |\phi|}{\partial x}) \tag{14}$$

Eq. 12 guarantees the maximum mobility for edge-on growth front with an ordered surface ($\phi \perp n$) and flat-on growth front with dendrite-like $k$-fold symmetry. Because no coarsening behavior is observed within the crystallization time-scale in our experiments, the mobility is set to be 0 for the crystalline region with a certain threshold on $|\phi|$ given by $\bar{c}$ and $\tilde{c}$ in Eq. 13.

A spatially correlated Gaussian noise is used here for the construction of stochastic fluctuations $\eta$ to reflect the fact that the orientation of the initially amorphous polymer is correlated

within certain length scale $l$. In addition, the fluctuation will only occur at the growth front with ordered surface such that the secondary nucleation on the side of crystalline lamellae is suppressed.

$$< \eta(r,t) > \quad = \quad 0, \quad < \eta(r,t), \eta(r',t') >= \tilde{\eta}^2 R(r,r';l)\delta(t-t') \tag{15}$$

$$R(r,r';l) \quad = \quad \frac{1}{2\pi l^2} \exp\left(\frac{-|r-r'|^2}{2l^2}\right) \tag{16}$$

$$\tilde{\eta} \quad = \quad 4|\phi|(1-|\phi|)\left(1-|\frac{\phi \cdot n}{|\phi||n|}|\right)\sqrt{2k_B T \tilde{M}} \tag{17}$$

Numerical simulations are initialized with a small crystalline seed centered within the amorphous droplet domains (where $\Delta = 2$). Representative values of nondimensionalized parameters we used in the simulations are: $N_x = N_y = 1024$, $\Delta t = 4 \times 10^{-7}$, $M_{max} = 5 \times 10^5$, $\Delta x = 0.01$, $\epsilon^2 = 2 \times 10^{-5}$, $\alpha = 0.9$, $\delta_\beta = 2$, $k = 4$, $\epsilon_2 = 2$, $\epsilon_4 = 2$, $\epsilon_{higher} = 10^{-9}$, $D_u = 20$, $b_1 = -0.005$, $b_2 = -0.01$, $\gamma = 10$, $k_B T = 1 \times 10^{-9}$, $\overline{c} = 0.95$, $\tilde{c} = 0.01$, $c_1 = 0.95$, $\lambda = 0$. During the numerical calculations, a nine-point stencil is employed to calculate all Laplacians while Fourier transforms are used for the stochastic fluctuations. Figure S1
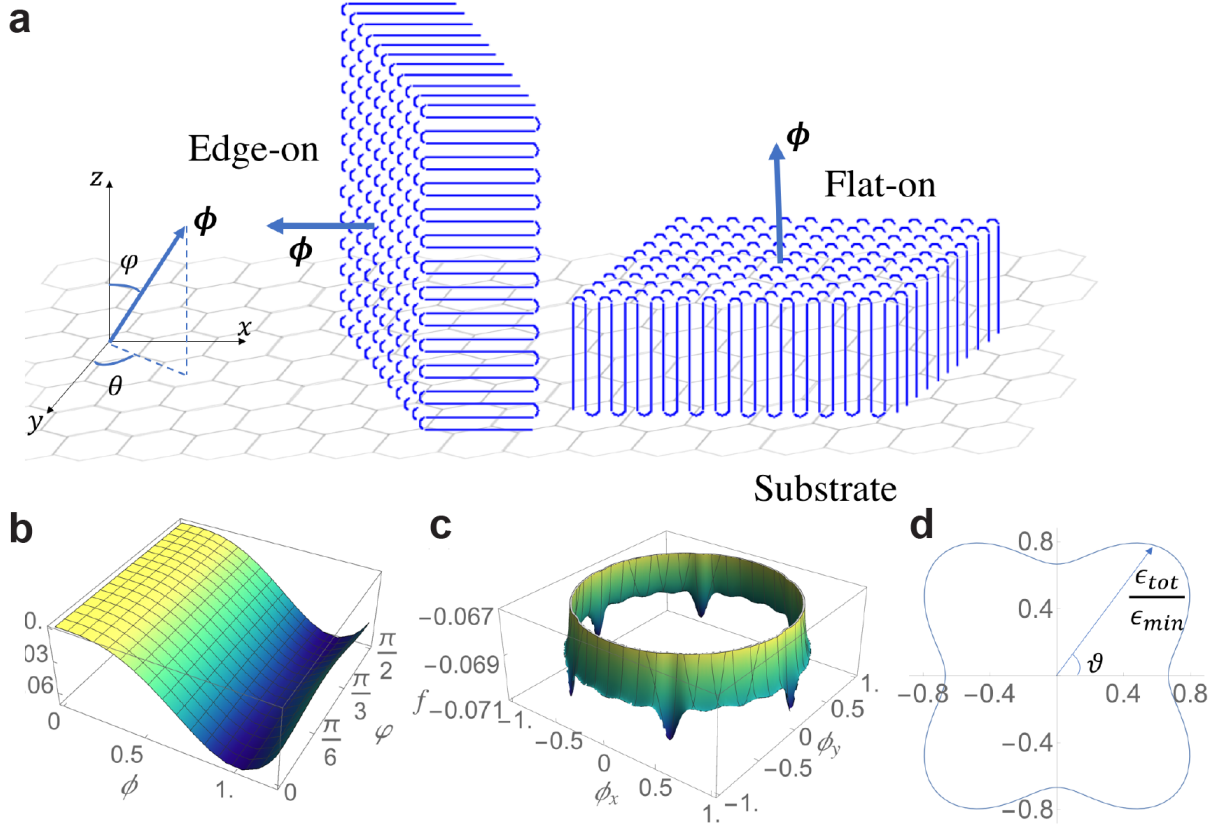
**Figure S1:** (a) Schematic showing the orientation of $\phi$ for edge-on and flat-on crystalline phases on a substrate and the corresponding orientation angles $\varphi$ and $\theta$. (b) The bulk free energy density with local minima at $|\phi| = 0, |\phi| = 1, \varphi = 0,$ and $\varphi = \pi/2$ (c) The six-fold symmetric bulk potential energy wells in the $x$–$y$ plane of $f$ to reflect the energetic benefit of epitaxial alignment as well as the preferred edge-on crystal orientation ($\varphi = \pi/2$). (d) Normalized anisotropic total interfacial energy $\epsilon_{tot}/\epsilon_{min}$ for different angles $\theta$.

# 4. Epitaxial relationship between PEO and muscovite mica

MAPLE permits the gentle deposition of polyethylene oxide films atop thin exfoliated flakes of muscovite mica, and this enables us to elucidate the nature of the epitaxial relationship between PEO and mica with selected area electron diffraction (SAED). Facile cleavage along the $(001)_{mica}$ basal plane exposes an atomically smooth surface,[2,3] upon which PEO is deposited. The crystal structure of mica is monoclinic, and its lattice parameters give it a quasi-hexagonal symmetry, as viewed from [001] in Figure S2c. This is because two families of planes, $\{020\}_{mica}$ and $\{110\}_{mica}$, have nearly identical interplanar spacings: $d_{\{020\}} = 4.50$ Å $\approx d_{\{110\}} = 4.49$ Å.[3–5] This quasi-hexagonal symmetry is illustrated by the SAED pattern for pristine mica in the left inset of Figure S2b. PEO has a monoclinic crystal structure in which the closest packed family planes is $\{120\}_{PEO}$, with $d_{\{120\}} = 4.63$ Å between adjacent polymer chains.[6,7] When viewed along the chain axis (Figure S2d), a four-fold symmetry is observed, similarly reflected by the SAED pattern in the right inset of Figure S2b.

In Figure S2b, an SAED pattern is shown for an electron beam incident from $[001]_{mica}$ onto a mica sample on which PEO is epitaxially crystallized. In addition to the six quasi-hexagonal spots corresponding to $\{020\}_{mica}$ and $\{110\}_{mica}$, two polymer diffraction peaks appear. Since edge-on PEO needles are aligned only along a single epitaxial direction within an SAED region, just two polymer diffraction peaks exist, corresponding to $(120)_{PEO}$ and $(1\bar{2}0)_{PEO}$ epitaxially oriented with $(110)_{mica}$ and $(1\bar{1}0)_{mica}$. Due to imperfect alignment of the edge-on crystals, the PEO diffraction appears as a band, more clearly shown in the zoom-in of Figure S2e. SAED measurements thus indicate that epitaxy occurs with the following orientation relationships: $(120) <120>_{PEO}$ // $(001) <110>_{mica}$ and $(120) <120>_{PEO}$ // $(001) <020>_{mica}$, with a 3.0% average lattice mismatch in both cases. Therefore, epitaxial PEO crystals are aligned with the chain axes of their semicrystalline lamellae oriented perpendicular to the six quasi-hexagonal directions of mica's cleave surface. The epitaxial relationship between $<110>_{mica}$ and $<120>_{PEO}$ is depicted in a view along the PEO chain axis in Figure S2d, where the double-headed blue arrow indicates equivalent directions, including in reciprocal space, for all sub-panels of Figure S2. This view clearly visualizes the direct correspondence between PEO chains and mica surface potassium ions, half of which are present upon cleavage.
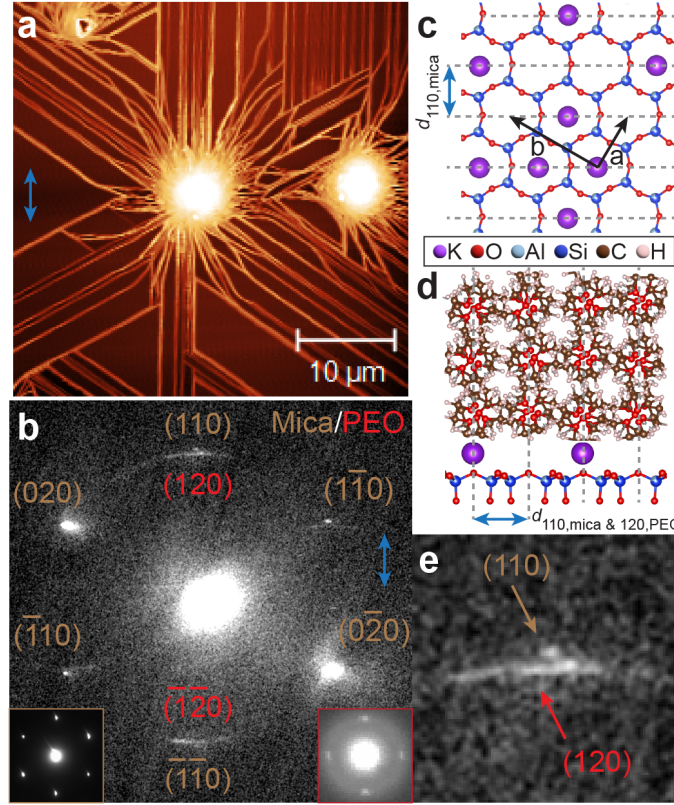
**Figure S2:** Structure of the epitaxial relationship between muscovite mica and polyethylene oxide. The blue double-headed arrows indicate equivalent directions in all sub-panels. (a) Representative AFM image of epitaxial needles emanating outwards in six directions from a central droplet. (b) Selected area electron diffraction pattern of PEO needles atop exfoliated sheets of mica, with $[001]_{mica}$ as the incident beam direction. Here, the blue double-headed arrow is arbitrarily chosen to represent $[110]_{mica}$. Tan-colored Miller indices refer to mica crystallographic planes, while red indices refer to PEO. The bottom-left inset depicts the diffraction pattern of pristine exfoliated mica, while the bottom right inset depicts the diffraction pattern of a flat-on PEO crystal, which exhibits four diffraction peaks. (c) Atomic structure model of the cleaved surface of mica, viewed from $[001]_{mica}$. The a and b vectors are the lattice basis vectors. The grey dotted lines indicate $(110)_{mica}$, one of the quasi-hexagonal six sets of planes along which epitaxy occurs. (d) Atomic structure model of PEO atop mica, viewed from along the PEO chain axis to illustrate the epitaxial relationship between PEO and mica. The grey dotted lines indicate both $(110)_{mica}$ and $(120)_{PEO}$. (e) Zoom-in to the $(110)_{mica}$ and $(120)_{PEO}$ diffraction patterns from panel (b). The upper dot is the diffraction peak of $(110)_{mica}$ while the lower band is the diffraction peak of $(120)_{PEO}$. Their aligned orientation and overlaid position indicates their epitaxial relationship.
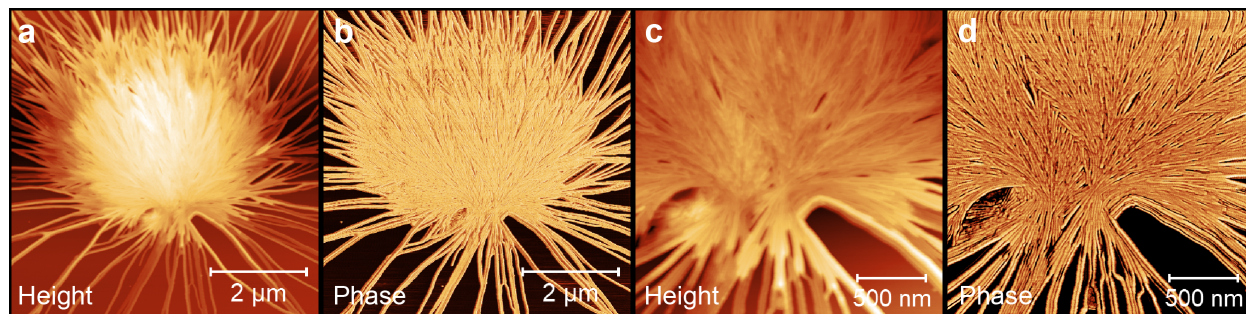
# 5. Supplementary Figures



**Figure S3:** AFM height and phase images of a PEO droplet deposited by MAPLE atop a muscovite mica substrate. (c) and (d) are zoomed-in AFM scans of the (a) and (b). The spherulitic structure is apparent in the phase image of panel (d).
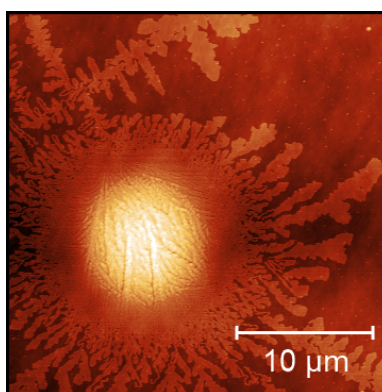


**Figure S4:** Example AFM image of PEO deposited by MAPLE from a 0.5% wt. target solution onto an Si wafer. No edge-on crystals are observed in any samples; only flat-on polymer crystals grow outside of the central droplet.
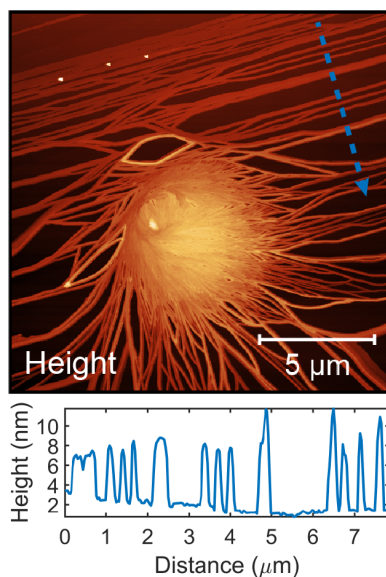
**Figure S5:** Height image of an individual crystalline droplet surrounded by epitaxial needles.
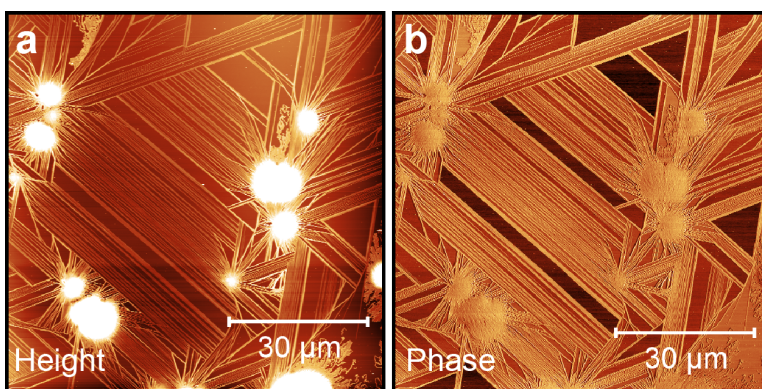


**Figure S6:** AFM height and phase images of PEO droplets deposited on mica. Additional examples of bounded regions containing amorphous nanolayers can be seen in (b), where different bounded regions exhibit different phase lags depending on the amount of residual material.
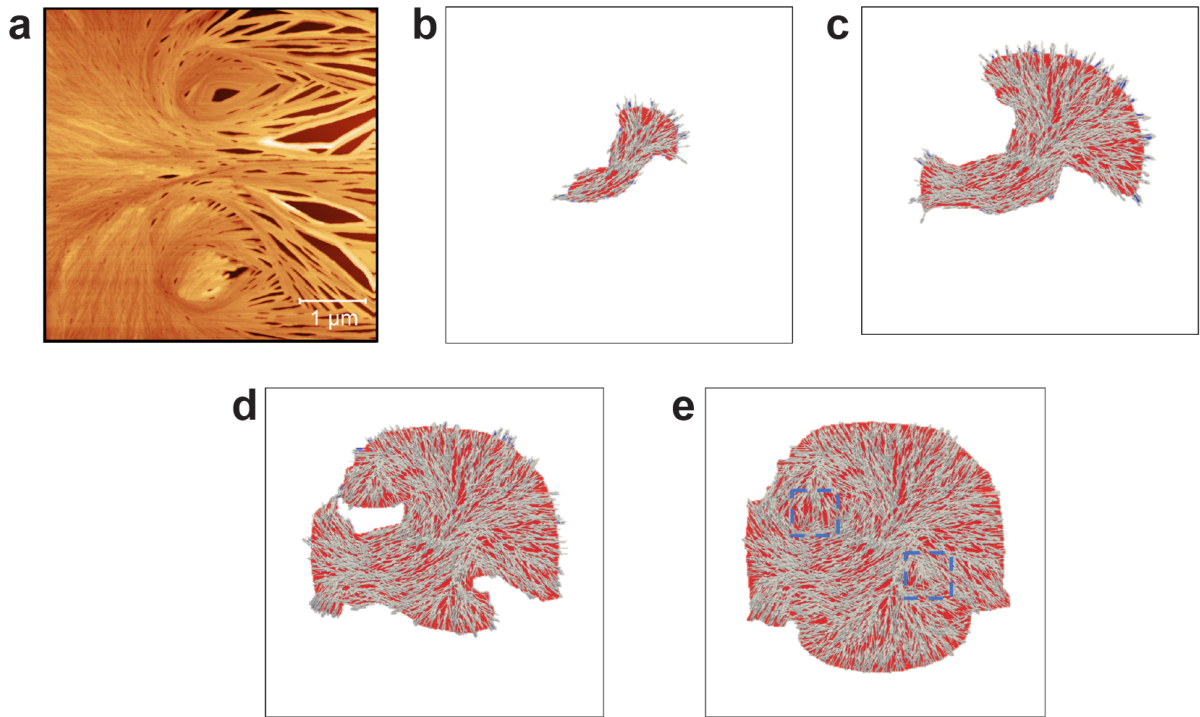
**Figure S7:** (a) AFM height image of a spherulitic "eye" structure at the primary crystal nucleation point, located at the edge of a PEO droplet deposited on mica. (b)-(e) Phase-field simulation of the formation procedure of the spherulite with the arrows denoting the highest-growth-rate direction of lamellae (the tip direction). The blue dashed squares in (a) and (e) indicate the location of the eyes formed during the crystallization.

# References

(1) Momma, K.; Izumi, F. VESTA 3 for three-dimensional visualization of crystal, volumetric and morphology data. *Journal of Applied Crystallography* **2011**, *44*, 1272–1276.

(2) Ostendorf, F.; Schmitz, C.; Hirth, S.; Kühnle, A.; Kolodziej, J. J.; Reichling, M. How flat is an air-cleaved mica surface? *Nanotechnology* **2008**, *19*.

(3) De Poel, W.; Pintea, S.; Drnec, J.; Carla, F.; Felici, R.; Mulder, P.; Elemans, J. A.; Van Enckevort, W. J.; Rowan, A. E.; Vlieg, E. Muscovite mica: Flatter than a pancake. *Surface Science* **2014**, *619*, 19–24.

(4) Baxter, R.; Hastings, N.; Law, A.; Glass, E. J. The nature of the air cleaved mica surface. *Animal Genetics* **2008**, *39*, 561–563.

(5) Richardson, S. M.; Richardson, J. W. Crystal structure of a pink muscovite from Archer's Post, Kenya: implications for reverse pleochroism in dioctahedral micas. *American Mineralogist* **1982**, *67*, 69–75.

(6) Zhang, G.; Cao, Y.; Jin, L.; Zheng, P.; Van Horn, R. M.; Lotz, B.; Cheng, S. Z.; Wang, W. Crystal growth pattern changes in low molecular weight poly(ethylene oxide) ultrathin films. *Polymer* **2011**, *52*, 1133–1140.

(7) Takahashi, Y.; Tadokoro, H. Structural Studies of Polyethers, (–(CH2)m–O–)n. X. Crystal Structure of Poly(ethylene oxide). *Macromolecules* **1973**, *6*, 672–675.